Phase diagram of manganese oxides

Ryo Maezono, Sumio Ishihara,* and Naoto Nagaosa
Department of Applied Physics, University of Tokyo, Bunkyo-ku, Tokyo 113, Japan

(Received 19 May 1998)

We study theoretically the phase diagram of perovskite manganites taking into account the double degeneracy of the e_g orbitals in a Mn^{3+} ion. A rich phase diagram is obtained in the mean-field theory at zero temperature as functions of x (hole concentration) and J_S (antiferromagnetic interaction between t_{2g} spins). The global features of the phase diagram are understood in terms of the superexchange and double-exchange interactions, which strongly depend on the types of occupied e_g orbitals. The strong electron correlation induces the orbital polarization, which controls the dimension of the conduction band. A sequential change of the spin and orbital structures with doping holes is consistent with the recent experiments. In particular, a metallic A-type (layered) antiferromagnetic state is found for $x \sim 0.5$ with the uniform $d_{x^2-y^2}$ orbital ordering. In this phase, calculated results suggest two-dimensional conduction and absence of the spin canting, which are observed experimentally. The effects of the Jahn-Teller distortion are also studied. [S0163-1829(98)01242-9]

I. INTRODUCTION

Doped manganites $R_{1-x}A_xMnO_3$ ($R =$ La, Pr, Nd, Sm; $A =$ Ca, Sr, Ba) have recently attracted considerable interest from the viewpoint of a close connection between the magnetism and the electric transport.[1–4] Theoretical studies of the double-exchange interaction were developed a long time ago[5–7] and explained the emergence of the ferromagnetism in doped manganites.[8] However, recent systematic experimental studies have revealed more rich phase diagrams in this system.

Observed phase diagrams of $La_{1-x}Sr_xMnO_3$ (wider bandwidth system) and of $Pr_{1-x}Sr_xMnO_3$ and $Nd_{1-x}Sr_xMnO_3$ (narrower bandwidth systems) are shown in Fig. 1.[3,9,10] Abbreviations used in Fig. 1 are PI (paramagnetic insulator), PM (paramagnetic metal), FI (ferromagnetic insulator), FM (ferromangetic metal), CNI, CAF (canted antiferromagnetic insulator), AFI (antiferromagnetic insulator), AFM (antiferromangetic metal), and COI (charge-ordered insulator). In the parent compound ($x = 0.0$), the layered antiferromagnetism (spin-A-type AF) accompanied with a distortion in the MnO_6 octahedron is realized.[11,12] By moderately doping holes, the insulator with spin-A-type AF changes into an insulator with a ferromagnetism (spin F type) around $x = 0.125$, and to a spin-F-type metal at $x \sim 0.175$ in $La_{1-x}Sr_xMnO_3$ [panel (a)].[3,13,14] A similar magnetic transition from A type to F type can be seen in panels (b) and (c). A metallic phase with spin-A-type AF was found recently to appear for $x > 0.52$ in $La_{1-x}Sr_xMnO_3$,[15] and for $x > 0.48$ in $Pr_{1-x}Sr_xMnO_3$ and $Nd_{1-x}Sr_xMnO_3$ [panels (b) and (c)].[9,10,16] With further increasing of x ($x \sim 0.6$), rod-type antiferromagnetism (spin-C-type AF) is found in $La_{1-x}Ca_xMnO_3$ (Ref. 11) and $Nd_{1-x}Sr_xMnO_3$ [panel (c)].[10] Finally, for $x = 1.0$, the three-dimensional AF (spin-G-type AF) is realized. In addition, in the narrower-band systems [panels (b) and (c)], the charge-ordered state accompanied by the spin ordering is recognized near the commensurate value of x ($x = 0.5$, 0.75, etc.),[17,18] where the orbital is also supposed to be ordered.

In order to reveal the origin of the unique magnetotransport in this system, it is essential to understand the above rich phase diagram. However, it cannot be explained by the conventional scenario based on the double-exchange interaction. This discrepancy should be attributed to ingredients neglected in the conventional theory, namely the anisotropic transfer intensity originated from the e_g orbital degrees of freedom, electron-electron interactions, and the electron-lattice interaction [Jahn-Teller (JT) effect]. Especially, in the narrower-band systems, the kinetic energy of e_g carriers is suppressed and the above interactions become more important. At $x = 0.0$, the spin and orbital structures have been studied theoretically by taking into account the above interactions since the pioneering works by Goodenough and Kanamori.[19,20] However, when we focus on the origin of the spin structure at $x = 0$, i.e., the A-type AF, and roles of the JT distortion on it, the situation is still controversial. In one side of the theoretical investigation, the spin ordering is attributed to the strong electron-electron interaction and the doubly degenerate e_g orbitals.[21–24] The ferromagnetic superexchange interaction, which is necessary to explain the spin alignment in the ab plane, is originated from the degenerate orbitals and the Hund coupling interaction between them.[19,20,25–27] Even without the JT effect, the A-type spin alignment is derived by the superexchange interaction and the anisotropy of the transfer integral due to the orbital ordering. However, a type of orbital ordering theoretically obtained disagrees with that expected from a type of JT distortion, i.e., $d_{3x^2-r^2}$ and $d_{3y^2-r^2}$. Another side of the theoretical investigation is based on the Hartree-Fock theory[28] and the first-principles band calculation base on the local-density approximation,[29] where the JT distortion is indispensable to reproduce the observed spin structure through introduction of the orbital polarization. Without the JT distortion, the system becomes a ferromagnetic metal.

As for the doped case ($x \neq 0$), the situation is even more controversial. An issue of main interest here is the origin of the colossal magnetoresistance (CMR) observed near the ferromagnetic transition temperature T_c. For this purpose identification of the dominant interactions is of primary impor-

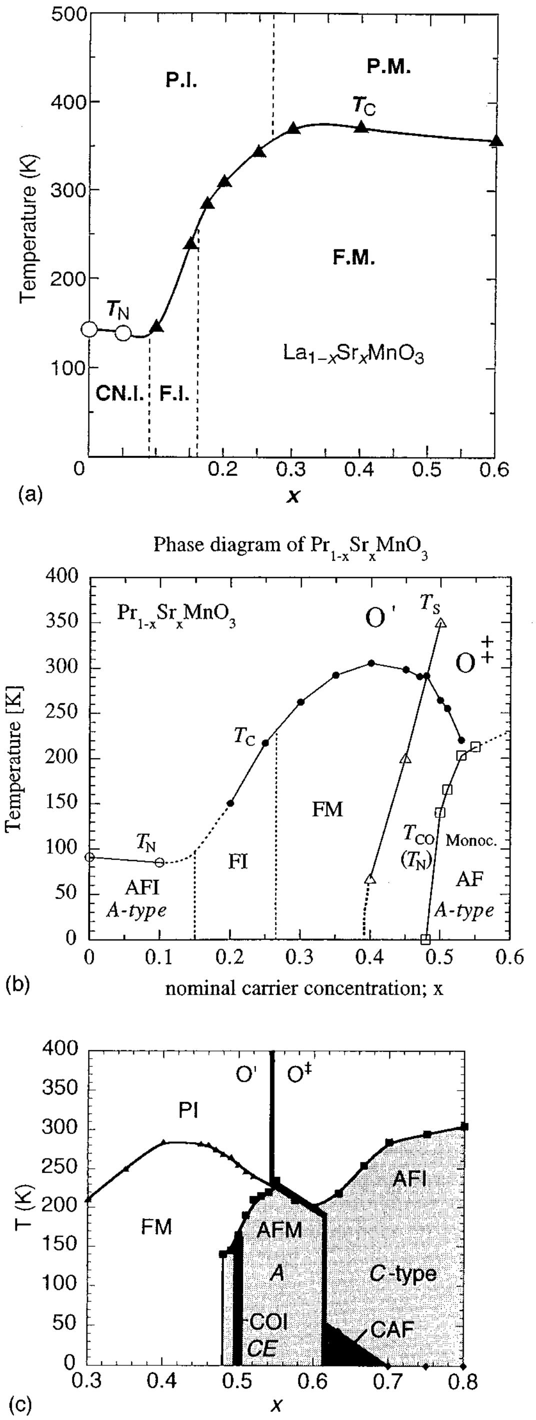

FIG. 1. Phase diagrams of (a) $La_{1-x}Sr_xMnO_3$ (Ref. 3), (b) $Pr_{1-x}Sr_xMnO_3$ (Ref. 9), and (c) $Nd_{1-x}Sr_xMnO_3$ (Ref. 10). Abbreviations used in figures are defined in the text.

tance. Millis *et al.*[30] attributed an insulating behavior of the resistivity $\rho(T)$ above T_c to the formation of the small JT polaron. They assumed the strong Hund's coupling, but the other Coulomb interactions were neglected. The characteristic JT interaction is about 1 eV which is comparable or smaller than the bandwidth. Then it is reasonable that the small-polaron formation disappears below T_c and $\rho(T)$ shows metallic behavior. However we argue that this picture does not explain the following anomalous features observed in the low-temperature ferromagnetic state ($T \ll T_c$): (i) $\rho(T)$ is fitted by $\rho(T)=\rho_0+AT^2$ with the coefficient A being large, i.e., $A \sim 500$ $\mu\Omega$ cm/K^2.[3] (ii) The optical conductivity $\sigma(\omega)$ is dominated by the incoherent part with a small Drude weight.[31] (iii) Photoemission experiments show only a small discontinuity at the Fermi edge.[32] We regard these features as signatures of the strong correlation in the doped Mott insulator and the Coulomb interactions remain strong even in the metallic state. Considering the strong Hund's coupling, which causes the perfect spin polarization, it is reasonable to assume the strong correlation between e_g electrons. In the ferromagnetic state, the orbital degrees of freedom play a similar role to that of spins in the usual doped Mott insulator. It is the additional ingredient important in the manganites.

In this paper we study a phase diagram of perovskite manganese oxides. The double degeneracy of the e_g orbital, the anisotropy of the transfer integral based on it, and the strong electron correlation are taken into account in the model. The spin and orbital phase diagram at zero temperature is obtained by the mean-field approximation. The sequential change of the spin structure with doping of holes, i.e., $A \rightarrow F \rightarrow A \rightarrow C \rightarrow G$, is well reproduced by the calculation. We found that the strong Coulomb interactions experimentally suggested induce the perfect orbital polarization which plays an essential role in determining the spin structure. The orbital structure is also changed with doping of holes and controls the dimensionality of the conduction bands. In particular, the metallic spin-A-type AF phase is found around $x \sim 0.5$ where the orbitals are aligned as $d_{x^2-y^2}$. In this phase, the interlayer electron transfer is forbidden both by the spin and orbital structures and the spin canting is absent. Both theoretical predictions are consistent with the recent experiments.[9,10] The role of the JT distortion in the undoped case is also studied.

In Sec. II, we introduce the model Hamiltonian and the formulation of the mean-field calculation. Results of the numerical calculation are presented in Sec. III. Section IV is devoted to discussion and conclusion including comparison with the previous works. A short version of this paper has been already published,[33] but this paper contains additional and more detailed results.

II. MODEL AND FORMULATION

We start with the Hamiltonian

$$H=H_K+H_{\mathrm{Hund}}+H_{\mathrm{on\,site}}+H_S, \tag{1}$$

where H_K is the kinetic energy of e_g electrons, H_{Hund} is the Hund coupling between e_g and t_{2g} spins, and $H_{\mathrm{on\,site}}$ represents the on-site Coulomb interactions between e_g electrons. t_{2g} spins are treated as the localized spins with $S=3/2$. The AF coupling between nearest neighboring t_{2g} spins is introduced in H_S to reproduce the AF spin ordering observed at $x=1.0$. Using an operator $d_{i\sigma\gamma}^{\dagger}$ which creates an e_g electron with spin σ $(=\uparrow,\downarrow)$ in the orbital $\gamma[=a(d_{x^2-y^2}),b(d_{3z^2-r^2})]$ at site i, each term of Eq. (1) is given by

$$H_K=\sum_{\sigma\gamma\gamma'\langle ij\rangle} t_{ij}^{\gamma\gamma'} d_{i\sigma\gamma}^{\dagger} d_{j\sigma\gamma'}, \tag{2}$$

$$H_{\mathrm{Hund}}=-J_H\sum_i \vec{S}_{t_{2g}i}\cdot\vec{S}_{e_g i}, \tag{3}$$

and

$$H_S=J_S\sum_{\langle ij\rangle} \vec{S}_{t_{2g}i}\cdot\vec{S}_{t_{2g}j}. \tag{4}$$

$t_{ij}^{\gamma\gamma'}$ in H_K is the electron transfer intensity between nearest-neighboring sites and it depends on kind of occupied orbital and the direction of a bond as follows:[34]

$$t_{ii+x}^{\gamma\gamma'}=t_0\begin{pmatrix} -\frac{3}{4} & \frac{\sqrt{3}}{4} \\ \frac{\sqrt{3}}{4} & -\frac{1}{4} \end{pmatrix}, \tag{5}$$

$$t_{ii+y}^{\gamma\gamma'}=t_0\begin{pmatrix} -\frac{3}{4} & -\frac{\sqrt{3}}{4} \\ -\frac{\sqrt{3}}{4} & -\frac{1}{4} \end{pmatrix}, \tag{6}$$

and

$$t_{ii+z}^{\gamma\gamma'}=t_0\begin{pmatrix} 0 & 0 \\ 0 & -1 \end{pmatrix}. \tag{7}$$

t_0 is the electron transfer intensity between $d_{3z^2-r^2}$ orbitals along the z direction. The spin operator for the e_g electron is defined as $\vec{S}_{e_g i}=\frac{1}{2}\Sigma_{\gamma\alpha\beta}d_{i\gamma\alpha}^{\dagger}\vec{\sigma}_{\alpha\beta}d_{i\gamma\beta}$ with the Pauli matrices $\vec{\sigma}_{\alpha\beta}$. $\vec{S}_{t_{2g}i}$ denotes the localized t_{2g} spin on the i site with $S=3/2$. The last term in the Hamiltonian $H_{\text{on site}}$ consists of the following three contributions:

$$H_{\text{on site}}=H_U+H_{U'}+H_J, \tag{8}$$

where H_U and $H_{U'}$ are the intra- and the interorbital Coulomb interactions, respectively, and H_J denotes the interorbital exchange interaction. Each term is represented as

$$H_U=U\sum_{j\gamma} n_{j\gamma\uparrow}n_{j\gamma\downarrow}, \tag{9}$$

$$H_{U'}=U'\sum_{j\sigma\sigma'} n_{ja\sigma}n_{jb\sigma'}, \tag{10}$$

and

$$H_J=J\sum_{j\sigma\sigma'} d_{ja\sigma}^{\dagger}d_{jb\sigma'}^{\dagger}d_{ja\sigma'}d_{jb\sigma}, \tag{11}$$

with $n_{j\gamma\sigma}=d_{j\sigma\gamma}^{\dagger}d_{j\sigma\gamma}$ and $n_{j\gamma}=\Sigma_\sigma n_{j\gamma\sigma}$. There should be some relation between these three energy parameters U, U', and J. In the case of the ionic crystal, this relation is given by the Racah parameters. Based on this relation, we assume $U=U'+J$ in our case.[34] By using the spin operator for the e_g electrons and the isospin operator describing the orbital degrees of freedom, defined as

$$\vec{T}_i=\frac{1}{2}\sum_{\gamma\gamma'\sigma} d_{i\gamma\sigma}^{\dagger}\vec{\sigma}_{\gamma\gamma'}d_{i\gamma'\sigma}, \tag{12}$$

$H_{\text{on site}}$ can be rewritten by[34]

$$H_{\text{on site}}=-\sum_i (\tilde{\beta}\vec{T}_i^2+\tilde{\alpha}\vec{S}_{e_g i}^2). \tag{13}$$

Coefficients of the spin and isospin operators, i.e., $\tilde{\alpha}$ and $\tilde{\beta}$, are given by

$$\tilde{\alpha}=U-\frac{J}{2}>0, \tag{14}$$

and

$$\tilde{\beta}=U-\frac{3J}{2}>0. \tag{15}$$

The minus sign in Eq. (13) means that the Coulomb interactions induce both spin and orbital (isospin) moments. In the path-integral representation, the expression of the grand partition function is represented as

$$\Xi=\int\prod_i D\vec{S}_{t_{2g}i}D\overline{d}_{i\gamma\sigma}Dd_{i\gamma\sigma}\exp\left\{-\int d\tau L(\tau)\right\}, \tag{16}$$

with

$$L(\tau)=H(\tau)+\sum_{\sigma\gamma i}\overline{d}_{\sigma\gamma i}(\tau)(\partial_\tau-\mu)d_{\sigma\gamma i}(\tau), \tag{17}$$

where τ is the imaginary time introduced in the path-integral formalism, and $\overline{d}_{i\gamma\sigma}$ and $d_{i\gamma\sigma}$ are the Grassmann variables corresponding to the operators $d_{i\gamma\sigma}^{\dagger}$ and $d_{i\gamma\sigma}$, respectively. By utilizing Eq. (13), the Hamiltonian is rewritten as

$$H(\tau)=-\tilde{\alpha}\sum_i\left(\vec{S}_{e_g i}+\frac{J_H}{2\tilde{\alpha}}\vec{S}_{t_{2g}i}\right)^2+\frac{J_H^2}{4\tilde{\alpha}}\sum_i\vec{S}_{t_{2g}i}^2$$
$$+J_S\sum_{\langle ij\rangle}\vec{S}_{t_{2g}i}\cdot\vec{S}_{t_{2g}j}-\tilde{\beta}\sum_i\vec{T}_i^2+H_K. \tag{18}$$

The bilinear terms with respect to the spin and isospin operators in the Hamiltonian are decoupled by introducing two kinds of auxiliary fields through the Stratonovich-Hubbard transformation. Then the partition function is rewritten as

$$\Xi=\int\prod_i D\vec{S}_{t_{2g}i}D\overline{d}_{i\gamma\sigma}Dd_{i\gamma\sigma}D\overrightarrow{\varphi_{Si}}\overrightarrow{\varphi_{Ti}}e^{-\int d\tau(L_d+L_{\vec{\varphi}})} \tag{19}$$

with

$$L_d=\sum_{\sigma\gamma i}\overline{d}_{\sigma\gamma i}(\tau)(\partial_\tau-\mu)d_{\sigma\gamma i}(\tau)$$
$$+\sum_{\sigma\gamma\gamma'\langle ij\rangle}t_{ij}^{\gamma\gamma'}\overline{d}_{\sigma\gamma i}(\tau)d_{\sigma\gamma' j}(\tau)$$
$$-2\tilde{\alpha}\sum_i\vec{S}_{e_g i}(\tau)\cdot\vec{\varphi}_{Si}(\tau)-2\tilde{\beta}\sum_i\vec{T}_i(\tau)\cdot\vec{\varphi}_{Ti}(\tau), \tag{20}$$

and

$$L_{\vec{\varphi}}=J_S\sum_{\langle ij\rangle}\vec{S}_{t_{2g}i}(\tau)\cdot\vec{S}_{t_{2g}j}(\tau)-J_H\sum_i\vec{S}_{t_{2g}i}(\tau)\vec{\varphi}_{Si}(\tau)+\tilde{\alpha}\sum_i\vec{\varphi}^2_{Si}(\tau)+\tilde{\beta}\sum_i\vec{\varphi}^2_{Ti}(\tau). \tag{21}$$

Being based on the above formulas [Eqs. (19)–(21)], we introduce the mean-field approximation at this stage. At first, we consider the part of the Hamiltonian which describes the t_{2g} spin system, that is, the first and second terms in the right-hand side in Eq. (21). The mean-field solution in this system is given by

$$\langle\vec{S}_{t_{2gi}}\rangle=S\frac{\overline{\vec{\phi}_i}}{|\overline{\vec{\phi}_i}|}, \tag{22}$$

where $\overline{\vec{\phi}_i}$ is the solution of the following mean-field equation:

$$\overline{\vec{\phi}_i}=-2J_S\sum_j\frac{S\overline{\vec{\phi}_j}}{\overline{\phi_j}}+J_H\vec{\varphi}_{Si}. \tag{23}$$

By replacing the spin operator for the t_{2g} spins by $\langle\vec{S}_{t_{2g,i}}\rangle$, $L_{\vec{\varphi}}$ in Eq. (21) is given by

$$L_{\vec{\varphi}}=-J_H\sum_i\langle\vec{S}_{t_{2g}i}\rangle\vec{\varphi}_{Si}(\tau)+J_S\sum_{\langle ij\rangle}\langle\vec{S}_{t_{2g}i}\rangle\langle\vec{S}_{t_{2g}j}\rangle+\tilde{\beta}\sum_i\vec{\varphi}^2_{Ti}+\tilde{\alpha}\sum_i\vec{\varphi}^2_{Si}. \tag{24}$$

Next, we focus on L_d in Eq. (20). By using the momentum representation:

$$d_{\sigma\gamma' j}(\tau)=\frac{1}{\sqrt{\beta N}}\sum_k\sum_n d_{\sigma\gamma'}(k,\omega_n)e^{i\vec{k}\cdot\vec{R}_j-i\omega_n\tau}, \tag{25}$$

and

$$\varphi_{xj}(\tau)=\frac{1}{\sqrt{\beta N}}\sum_k\sum_n\varphi_x(k,\omega_n)e^{i\vec{k}\cdot\vec{R}_j-i\omega_n\tau}, \tag{26}$$

for $x=S$ and T, we have

$$\int d\tau L_d(\tau)=\sum_{kk';nn'}\sum_{\gamma\gamma';\alpha\beta}\overline{d}_{\alpha\gamma}(k,\omega_n)\times G^{-1}_{kk';nn';\gamma\gamma';\alpha\beta}d_{\beta\gamma'}(k',\omega_{n'}), \tag{27}$$

where ω_n is the Matsubara frequency for the fermion and the $G_{kk';nn';\gamma\gamma';\alpha\beta}$ is the Green function of the e_g electron defined by

$$\begin{aligned}G^{-1}_{kk';nn';\gamma\gamma';\alpha\beta}=&(-i\omega_n-\mu)\delta_{nn'}\delta_{\alpha\beta}\delta_{\gamma\gamma'}\delta_{kk'}\\&+\varepsilon_k^{\gamma\gamma'}\delta_{kk'}\delta_{nn'}\delta_{\alpha\beta}\\&-\frac{\tilde{\alpha}}{\sqrt{\beta N}}\vec{\sigma}_{\alpha\beta}\cdot\vec{\varphi}_S(k-k',\omega_n-\omega_{n'})\delta_{\gamma\gamma'}\\&-\frac{\tilde{\beta}}{\sqrt{\beta N}}\vec{\sigma}_{\gamma\gamma'}\cdot\vec{\varphi}_T(k-k',\omega_n-\omega_{n'})\delta_{\alpha\beta},\end{aligned} \tag{28}$$

with

$$\frac{1}{N}\sum_{\langle ij\rangle}t_{ij}^{\gamma\gamma'}e^{-i\vec{k}\vec{R}_i+i\vec{k}'\vec{R}_j}=\varepsilon_k^{\gamma\gamma'}\delta_{kk'}. \tag{29}$$

After integrating over the Grassman variable, the partition function is rewritten as

$$\Xi=\int D\{\varphi\}\exp\left(\mathrm{Tr}\ \ln G^{-1}_{kk';nn';\gamma\gamma';\alpha\beta}-\int d\tau L_{\vec{\varphi}}\right)\equiv e^{-\beta(F-\mu N)}. \tag{30}$$

Then we adopt the mean-field approximation by replacing the two kinds of auxiliary field, i.e., $\vec{\varphi}_S$ and $\vec{\varphi}_T$ by their values at the saddle point $\overline{\vec{\varphi}_S}$ and $\overline{\vec{\varphi}_T}$. Finally, we obtain the expression for the free energy in the mean-field approximation as

$$F=L_{\vec{\varphi}}|_{\{\varphi_x\}=\{\overline{\varphi_x}\}}-\frac{1}{\beta}\sum_\nu\ln[1+\exp\{-\beta(E^{(\nu)}-\mu)\}]_{\{\varphi_x\}=\{\overline{\varphi_x}\}}+\mu N, \tag{31}$$

where $E^{(\nu)}$ is the νth eigenvalue of $M_{kk';\gamma\gamma';\alpha\beta}$ defined by

$$M_{kk';\gamma\gamma';\alpha\beta}=\varepsilon_k^{\gamma\gamma'}\delta_{kk'}\delta_{\alpha\beta}-\frac{\tilde{\alpha}}{\sqrt{N}}\vec{\sigma}_{\alpha\beta}\cdot\vec{\varphi}_S(k-k')\delta_{\gamma\gamma'}-\frac{\tilde{\beta}}{\sqrt{N}}\vec{\sigma}_{\gamma\gamma'}\cdot\vec{\varphi}_T(k-k')\delta_{\alpha\beta}. \tag{32}$$

The chemical potential μ is determined by the following condition:

$$(1-x)=\frac{1}{N}\sum_\nu f(E^{(\nu)}-\mu), \tag{33}$$

in terms of the doping concentration x. $f(x)$ is the Fermi distribution function.

By using the above expression of the free energy, we numerically calculate the spin and orbital phase diagram at zero temperature. We consider four kinds of spin alignment in the cubic cell: F, A, C, and G type. The possibility of the spin canting is also discussed later. As for the orbital degrees, their ordering is represented by the alignment of the isospin. We specify the orbital state by the angle in the orbital space as follows:

$$|\theta\rangle = \cos\frac{\theta}{2}|d_{x^2-y^2}\rangle + \sin\frac{\theta}{2}|d_{3z^2-r^2}\rangle, \tag{34}$$

which describes the direction of the isospin moment

$$\vec{T} = (-\sin\,\theta, 0, \cos\,\theta). \tag{35}$$

We also consider four types of orbital ordering, i.e., F, A, C, G type, in the cubic cell. The angle in the orbital space θ is varied for each sublattice, and these are denoted as θ_I and θ_{II} in the I and II sublattices, respectively. Henceforth, we often use a notation such as, orbital G:$(3x^2-r^2)/(3y^2-r^2) = (G:\pi/3,-\pi/3)$, through the relations

$$|d_{3x^2-r^2}\rangle = \cos\frac{(\pi/3)}{2}|d_{x^2-y^2}\rangle + \sin\frac{(\pi/3)}{2}|d_{3z^2-r^2}\rangle, \tag{36}$$

and

$$|d_{3y^2-r^2}\rangle = \cos\frac{(-\pi/3)}{2}|d_{x^2-y^2}\rangle + \sin\frac{(-\pi/3)}{2}|d_{3z^2-r^2}\rangle. \tag{37}$$

Therefore, we consider the 4 (spin)×4 (orbital) types of ordering with (θ_I, θ_{II}), and numerically compare the free energy between them.

III. NUMERICAL RESULTS

A. Parameters in the model

The values of the energy parameters $\tilde{\alpha}, \tilde{\beta}, J_H, J_S, t_0$, used in the numerical calculation are chosen as follows. In LaMnO$_3$, t_0 is estimated by the photoemission experiments to be $t_0 \sim 0.72$ eV,[35] which we choose the unit of the energy below $(t_0 = 1)$. By employing $U = 6.3$ eV and $J = J_H = 1.0$ eV as those relevant to the actual manganese oxides,[35] parameters for the electron-electron interactions in the present model are $\tilde{\alpha} = 8.1, \tilde{\beta} = 6.67$ $(\tilde{\alpha}/\tilde{\beta} = 1.21)$. The numerical calculation are also performed by using different sets of energy parameters in order to compare the previous works.[21–24] There, the effective Hamiltonians are derived by excluding the doubly occupied state in the e_g orbitals. The superexchange interaction between nearest-neighboring spin and orbital in these models are characterized by the energy in the intermediate states in the perturbation process. There are three kinds of intermediate states,[25–27,21] i.e., the two electrons occupy (1) the different orbitals with the parallel spin (the energy is $U' - J$), (2) the different ones with the antiparallel spins $(U' + J)$, and (3) the same orbital (U). The connection between these energies and the present energy parameters are roughly estimated as $U' - J \sim \tilde{\beta}$, $U \sim \tilde{\alpha}$, and $U' + J \sim \tilde{\alpha} + \tilde{\beta}$ from Eq. (13). Koshibae *et al.*[23] discussed the orbital ordering at $x = 0$ by using the exact diagonalization method in the limit of $U' - J \ll U, U' + J$ corresponding to $\tilde{\alpha}/\tilde{\beta} \gg 1$. Shiina *et al.*[24] also studies the spin and orbital structure in a wide range of parameters. In order to compare the above results, we show the two cases, that is, [case (A)] with $\tilde{\alpha} = 70$ and $\tilde{\beta} = 2.5 (\tilde{\alpha}/\tilde{\beta} \gg 1)$, and [case (B)] with $\tilde{\alpha} = 8.1$ and $\tilde{\beta} = 6.67$.

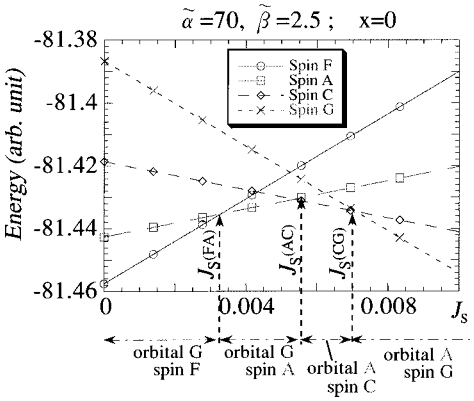

FIG. 2. Free energies for each spin alignment as a function of the antiferromagnetic interaction between t_{2g} spins J_S at $x = 0$. The energy parameters are chosen to be $\tilde{\alpha} = 70$ and $\tilde{\beta} = 2.5$ [case (A)]. Orbital structures are also noted.

B. Undoped $(x = 0)$ case

Let us consider the undoped case. In Fig. 2, we show the calculated free energy $F(J_S, x = 0)$ at $x = 0$ as a function of J_S for each spin alignment in the case of $\tilde{\alpha}/\tilde{\beta} \gg 1$ [case (A)]. In each spin alignment, the orbital structure is optimized. In the case of $J_S = 0$, the F-type spin alignment is favored due to the ferromagnetic superexchange interaction under the doubly degenerate orbital.[25–27] With increasing J_S, the stable spin structure is changed from F to A, C, and finally G type. This sequential change of the spin structure is consistent with the theoretical studies based on the effective Hamiltonian[22,23] in the limit $\tilde{\alpha}/\tilde{\beta} \gg 1$.

Spin and orbital structures are dependent on J_S and these are depicted in Fig. 3. Rearrangement of the orbital structure with changing J_S, which was previously pointed out,[23] is also found.

It is worth noting that the orbital structures also depend on the ratio $\tilde{\alpha}/\tilde{\beta}$. In Fig. 4, the angle in isospin space (θ_I, θ_{II}) obtained in the spin-A phase is presented. For $\tilde{\alpha}/\tilde{\beta} \gg 1$ the configuration $(\theta_I, \theta_{II}) = (90, -90)$ is obtained as the stable orbital structure. In this orbital ordering, the energy gain due to the superexchange process in the ferromagnetic bonds, i.e., $t^2/(U' - J)$ takes its maximum. Here, t represents the effective electron transfer intensity in this superexchange

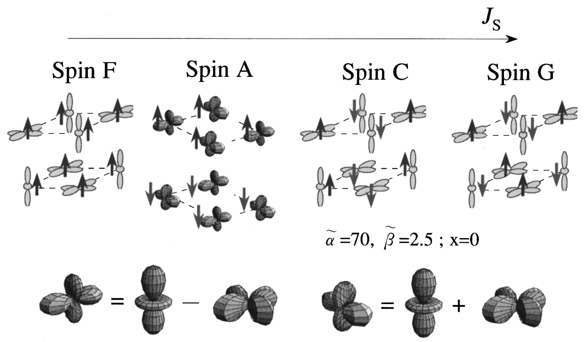

FIG. 3. Orbital structures at $x = 0$ as a function of the antiferromagnetic interaction between the t_{2g} spins J_S. The energy parameters are chosen to be $\tilde{\alpha} = 70$ and $\tilde{\beta} = 2.5$ [case (A)].

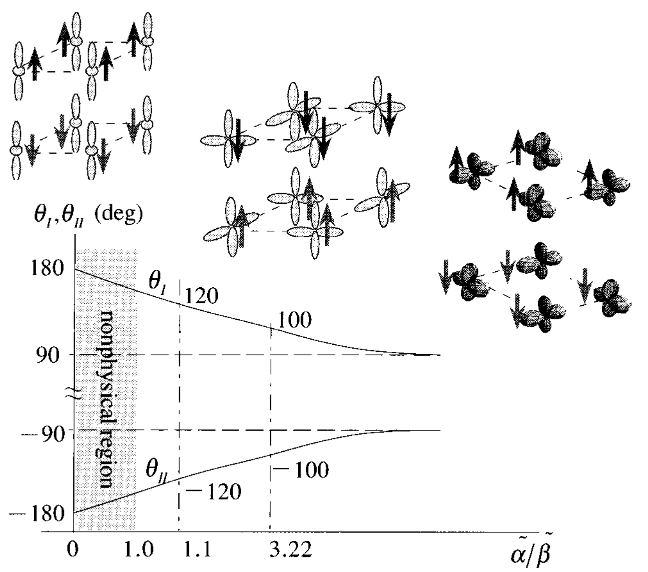

FIG. 4. Orbital structures in each sublattice at $x=0$ as a function of the electron-electron interaction parameters $\tilde{\alpha}/\tilde{\beta}$. The A-type spin alignment and the G-type orbital are assumed.

process including the effects of the orbital. On the other hand, for $\tilde{\alpha}/\tilde{\beta}\ll 1$, the superexchange processes in the AF bonds characterized by t^2/U and $t^2/(U'+J)$, become important. Actually $(\theta_I,\theta_{II})=(180,-180)$ is the most preferable configuration in this parameter region. Orbital $G{:}(3x^2-r^2)/(3y^2-r^2)$ $[(\theta_I,\theta_{II})=(60,-60)]$, which is supposed experimentally, cannot be the most stable for any $\tilde{\alpha}/\tilde{\beta}$. Rather than this structure, $G{:}(y^2-z^2)/(x^2-z^2)$ $[(\theta_I,\theta_{II})=(120,-120)]$ becomes stable around $\tilde{\alpha}/\tilde{\beta}\sim 1.1$.

These numerical results are understood by comparing the energy gains due to the superexchange processes between the two orbital configurations shown in Fig. 5. In processes with the energy $t^2/(U'+J)$ and $t^2/(U'-J)$, the transfer integral t between the occupied and the unoccupied orbital is concerned and it takes the same value for both configurations. On the other hand, in the process with $t^2/(U)$, relevant transfer is the one between the occupied orbitals along the c axis, which is always larger for the orbital: $G{:}(y^2-z^2)/(x^2-z^2)$ than that for orbital: $G{:}(3x^2-r^2)/(3y^2-r^2)$. Then there is no chance for the orbital $G{:}(3x^2-r^2)/(3y^2-r^2)$ to be the most stable structure for any $\tilde{\alpha}/\tilde{\beta}$, when only the superexchange mechanism is considered. Hence we conclude that the JT coupling plays an indispensable role for the $G{:}(3x^2-r^2)/(3y^2-r^2)$ orbital ordering at $x=0$, which we will discuss in the next section.

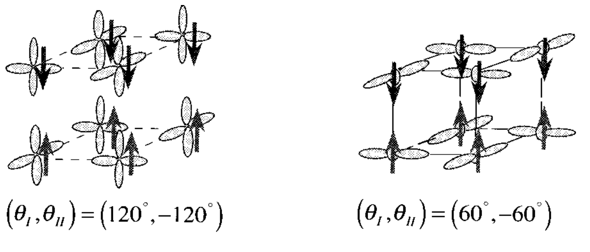
$(\theta_I,\theta_{II})=(120^\circ,-120^\circ)$ $(\theta_I,\theta_{II})=(60^\circ,-60^\circ)$

FIG. 5. Orbital orderings described as $(\theta_I,\theta_{II})=(120°, -120°)$ and $(60°,-60°)$, respectively.

In the vicinity of $\tilde{\alpha}/\tilde{\beta}=1$, A-type spin ordering appears even at $J_S=0$. This is consistent with the result obtained in the effective Hamiltonian at $x=0$.[24] In this region, the ferromagnetic interaction characterized by the energy $t^2/(U'-J)$ is suppressed, on the other hand, the AF ones with t^2/U and $t^2/(U'+J)$ are enhanced. When $\tilde{\alpha}/\tilde{\beta}$ approaches unity, fixing J_H as several eV, the spin-F structure at $J_S=0$ remains. It is concluded that the strong J_H plays an important role for the emergence of spin F at $J_S=0$.

C. Effects of the lattice distortion

Considering the experimental fact that the static JT distortion rapidly disappears around $x\sim 0.1$,[14,36] we examine the effect of the JT distortion on the spin and orbital phase diagram at $x=0$. The JT distortion directly affects the orbital configuration. As a result, the phase boundary between spin-F and spin AF phases is modified. To examine how the phase boundary is changed due to JT distortion, we chose the parameters as $\tilde{\alpha}/\tilde{\beta}\gg 1$, i.e., case (A), where the phase boundary exists at $x=0$ as shown in Fig. 9. The JT coupling is expressed as the coupling between the isospin operator $\vec{T}_j$ and the local lattice distortion $\vec{Q}_j$ as follows:[20]

$$H_{JT}=g\sum_j \vec{Q}_j\cdot\vec{T}_j+\frac{1}{2}\sum_j \omega_0^2\vec{Q}_j^2+\sum_j V(\vec{Q}_j), \tag{38}$$

where $V(\vec{Q}_j)$ is the anharmonic potential for $\vec{Q}_j$. Instead of minimizing the total energy, we assume $\vec{Q}_j$ as the experimentally observed one. In a $\mathrm{MnO_6}$ octahedron, $\vec{Q}_j$ is expressed as

$$\vec{Q}_j=r_j(\sin\Theta_j\hat{Q}_{x^2-y^2}+\cos\Theta_j\hat{Q}_{3z^2-r^2}), \tag{39}$$

where $\hat{Q}_{x^2-y^2(3z^2-r^2)}$ is the base of the normal coordinate of the cubic-symmetric system defined as $\hat{Q}_{x^2-y^2}=(\Delta_x-\Delta_y)/\sqrt{2}$ and $\hat{Q}_{3z^2-r^2}=(2\Delta_z-\Delta_x-\Delta_y)/\sqrt{6}$, and Δ_α denotes the elongation toward the α direction $(\alpha=x,y,z)$. In this notation, the first term in H_{JT}, which is termed $H_{\mathrm{el-ph}}$, is expressed as

$$H_{\mathrm{el-ph}}=+|g|\sum_j r_j\vec{v}_j\cdot\vec{T}_j, \tag{40}$$

with

$$\vec{v}_j=\begin{pmatrix}\sin\Theta_j\\ 0\\ \cos\Theta_j\end{pmatrix}. \tag{41}$$

We choose the sign of the coupling constant $+|g|$ so that the $d_{3z^2-r^2}$ orbital may be stabilized for $\hat{Q}_{3z^2-r^2}$, consistent with the negative charge of the oxygen ion. By the x-ray-diffraction experiment, it is confirmed that the $\mathrm{MnO_6}$ octahedron is elongated along the x or y direction and these octahedron are alternatively aligned in the ab plane.[12] In the present formula, it corresponds to $r_j=r$, $\Theta_j=-60°$ for the $j\in I$ sublattice and $\Theta_j=-60°$ for the $j\in II$ sublattice, i.e., $(\Theta_I,\Theta_{II})=(60°,-60°)$. By adding $H_{\mathrm{el-ph}}$ to the Hamiltonian introduced in the previous section [Eq. (1)], an additional molecular field for the isospin is introduced. As a result, the matrix element $M_{kk';\gamma\gamma';\alpha\beta}$ in Eq. (32) is modified as

$$M_{kk';\gamma\gamma';\alpha\beta}=\varepsilon_k^{\gamma\gamma'}\delta_{kk'}\delta_{\alpha\beta}-\tilde{\alpha}\vec{\sigma}_{\alpha\beta}\varphi_S\delta_{k-k'+q_S}\delta_{\gamma\gamma'}-\tilde{\beta}\left\{\left(\varphi_T^A-\frac{|g|r}{2\tilde{\beta}}v^A\right)\delta_{k-k'}+\left(\varphi_T^C-\frac{|g|r}{2\tilde{\beta}}v^C\right)\delta_{k-k'-q_\theta}\right\}(\sigma_z)_{\gamma\gamma'}\delta_{\alpha\beta}$$

$$-\tilde{\beta}\left\{\left(-\varphi_T^B-\frac{|g|r}{2\tilde{\beta}}v^{BD}\right)\delta_{k-k'}+\left(\varphi_T^B-\frac{|g|r}{2\tilde{\beta}}v^{BA}\right)\delta_{k-k'-q_\theta}\right\}(\sigma_x)_{\gamma\gamma'}\delta_{\alpha\beta}, \tag{42}$$

where

$$v^{BD}=-\cos(-120°)\sin\,\theta_I,$$

$$v^{BA}=\sin(-120°)\cos\,\theta_I,$$

$$v^A=\cos(-120°)\cos\,\theta_I,$$

$$v^C=\sin(-120°)\sin\,\theta_I,$$

$$\varphi_T^A=\varphi_T\sin^2\left(\frac{\theta_I-\theta_{II}}{2}\right),$$

$$\varphi_T^B=\varphi_T\cos\left(\frac{\theta_I-\theta_{II}}{2}\right)\sin\left(\frac{\theta_I-\theta_{II}}{2}\right),$$

$$\varphi_T^C=\varphi_T\cos^2\left(\frac{\theta_I-\theta_{II}}{2}\right),$$

and q_S (q_θ) denotes the wave vector for the spin (orbital) ordering. As well as the energy splitting between the two e_g orbitals due to the JT distortion [Eq. (40)], the distortion modifies the transfer integral through the modification of the bond length l between Mn and O ions. According to the pseudopotential theory,[37] the overlap integral between Mn $3d$ and O $2p$ orbitals is proportional to $l^{7/2}$. Therefore, the variations of the transfer integral between Mn $3d$ orbitals is evaluated by using the parameter $r(=r_j)$ as

$$t_{ii+\hat{x}(\hat{y})}^{\gamma\gamma'}(r)=\frac{t_{ii+\hat{x}(\hat{y})}^{\gamma\gamma'}(r=0)}{\sqrt{(1+2r)^7(1-r)^7}}, \tag{43}$$

and

$$t_{ii+\hat{z}}^{\gamma\gamma'}(r)=\frac{t_{ii+\hat{z}}^{\gamma\gamma'}(r=0)}{(1-r)^7}, \tag{44}$$

where we used the expression for the bond lengths in the elongated and shortened bonds as $l_{\mathrm{long}}=l_0(1+2r)$ and $l_{\mathrm{short}}=l_0(1-r)$, respectively. We also consider the change in the magnitude of J_S due to the JT distortion. With the relation $J_S(r)\propto t^2(r)$, the following relations are derived:

$$J_S^{x,y}(r)=\frac{J_S(r=0)}{(1+2r)^7(1-r)^7}, \tag{45}$$

and

$$J_S^z(r)=\frac{J_S(r=0)}{(1-r)^{14}}, \tag{46}$$

where $J_S^\alpha(r)$ is the superexchange interaction along the α direction with the distortion r. According to the x-ray-diffraction experiment,[12] bond lengths are reported as $l_{\mathrm{long}}=2.14$ Å and $l_{\mathrm{short}}=1.98$ or 1.96 Å corresponding to $r=0.028$. In order to distinguish the two kinds of modification due to the JT distortion, that is, the energy-level splitting and the modification of the transfer intensity, we examine these effects separately by two procedures as changing the value of g with fixing r and vice versa. Even for $g=0$, the modification of the transfer intensity lifts the degeneracy.

In Fig. 6, the stable orbital structure is shown as a function of the diagonal coupling gr with fixing r. For $g=0$, (θ_I,θ_{II}) is determined so as to lower the center of mass in the valence band. For sufficiently large g compared with t_0, JT distortion forces the orbital configuration to be $(\theta_I,\theta_{II})=(60,-60)$. The types of stable orbital are almost saturated as $(3x^2-r^2)/(3y^2-r^2)$ for $gr/t_0>0.5$. When the Coulomb interactions are not introduced, this value $gr/t_0\sim0.5$ is not enough to make the wave functions be $(3x^2-r^2)/(3y^2-r^2)$. Since the orbital is already polarized by the strong Coulomb interaction, the role of JT coupling is to rotate the direction of its polarization. It is much easier than to induce the polarization. We concluded that the wave function is almost $(3x^2-r^2)/(3y^2-r^2)$ at $x=0$, which, in principle, can be tested experimentally.[38,39]

In Fig. 7, the variation of the phase boundary between spin-F and spin-A phases are presented as functions of r and gr. The value of the superexchange interaction at the boundary is termed $J_S(FA)$, hereafter. In the case of $g=0$ [Fig. 7(a)], spin F is stabilized with increasing r. This is reasonable because the modification of the transfer intensity, described by Eqs. (43) and (44), enhances the ferromagnetic superexchange interaction along the c axis. On the other hand, introducing the energy splitting represented by gr with fixing r stabilizes the spin-A structure [Fig. 7(b)]. In order to understand this result, we estimate the energy gain due to the

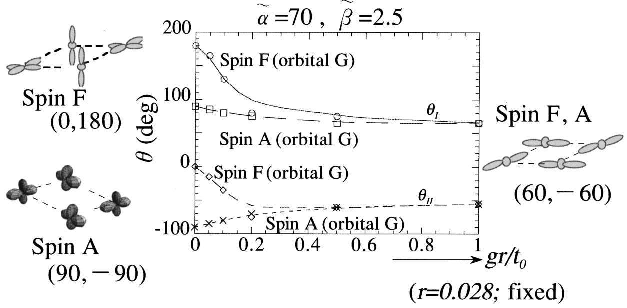

FIG. 6. Orbital structures in each sublattice as a function of magnitude of the JT splitting gr/t_0. The energy parameters are chosen to be $\tilde{\alpha}=70$ and $\tilde{\beta}=2.5$ [case (A)]. r is fixed at 0.028.

energy splitting as follows. The energy difference between the spin-F and spin-A phases is represented as

$$2S^2 J_S(FA;g)=E_A(g)-E_F(g), \tag{47}$$

where $E_{A(F)}(g)$ is the energy for the spin-$F(A)$ with the JT coupling g, and $J_S(FA;g)$ is the superexchange interaction at the phase boundary. The prefactor 2 in the left-hand side comes from the difference of the number of antiferromagnetic bonds between two phases. By using this expression, the change of the phase boundary between the $g=0$ and $g=\infty$ is estimated by

$$\begin{aligned}2S^2[J_S(FA;g=0)-J_S(FA;g=\infty)]&\\ =[E_A(g=0)-E_A(g=\infty)]&\\ -[E_F(g=0)-E_F(g=\infty)].&\end{aligned} \tag{48}$$

When the right-hand side of Eq. (49) is positive, the phase boundary $J_S(FA;g)$ is increased with decreasing g. Because the ferromagnetic superexchange interaction is only relevant at $x=0$ with the condition $\tilde{\alpha}/\tilde{\beta}\gg 1, E_{F(A)}(g)$ is proportional to the sum of the square of the transfer intensity between the nearest-neighboring occupied and unoccupied orbitals $[t_{o-u}(g)]$, that is,

$$E_{F(A)}(g)\propto-\sum_{\text{Ferro bonds}} t^2_{o-u}(g), \tag{49}$$

where $\Sigma_{\text{Ferro bonds}}$ implies the summation over the ferromagnetic bonds. These quantities are tabulated in Fig. 8. As a result, we obtain

$$\begin{aligned}&2S^2[J_S(FA;g=0)-J_S(FA;g=\infty)]\\ &\quad\propto-(I^{A,g=0}_{xy}-I^{A,g=\infty}_{xy})\\ &\qquad+\{(I^{F,g=0}_{xy}-I^{F,g=\infty}_{xy})+(I^{F,g=0}_{z}-I^{F,g=\infty}_{z})\}\\ &\quad=0.875>0,\end{aligned} \tag{50}$$

with

$$I_{xy}=\frac{1}{2}\left\{\sum (t^x_{o-u})^2+\sum (t^y_{o-u})^2\right\},$$

$$I_z=\frac{1}{2}\left\{\sum (t^z_{o-u})^2\right\}.$$

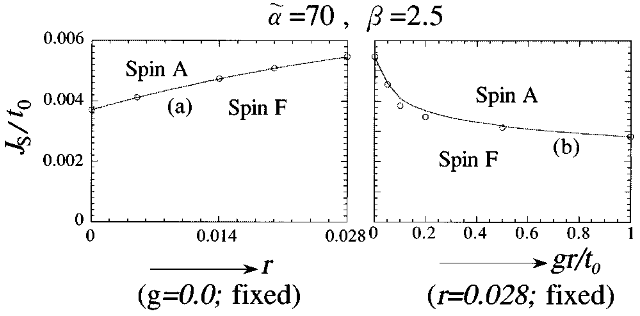

FIG. 7. Variation of the phase boundary between spin-F and spin-A phases as a function of (a) the magnitude of the JT distortion r fixing the JT splitting at $g=0$ (left-hand side panel), and (b) the JT splitting gr/t_0 fixing the magnitude of the distortion at $r=0.028$ (right-hand side panel).

		g=0	$g\to\infty$
Spin F		(G; 0,-180)	(G; 60,-60)
	intraplane	$I^{F,g=0}_{xv}=1.25/2$ (per bond)	$I^{F,g=\infty}_{xv}=1.5/2$ (per bond)
	intraplane	$I^{F,g=0}_{z}=1.0$ (per bond)	$I^{F,g=\infty}_{z}=0.375$ (per bond)
Spin A		(G; 90,-90)	(G; 60,-60)
	intraplane	$I^{A,g=0}_{xv}=1.75/2$ (per bond)	$I^{A,g=\infty}_{xv}=1.5/2$ (per bond)

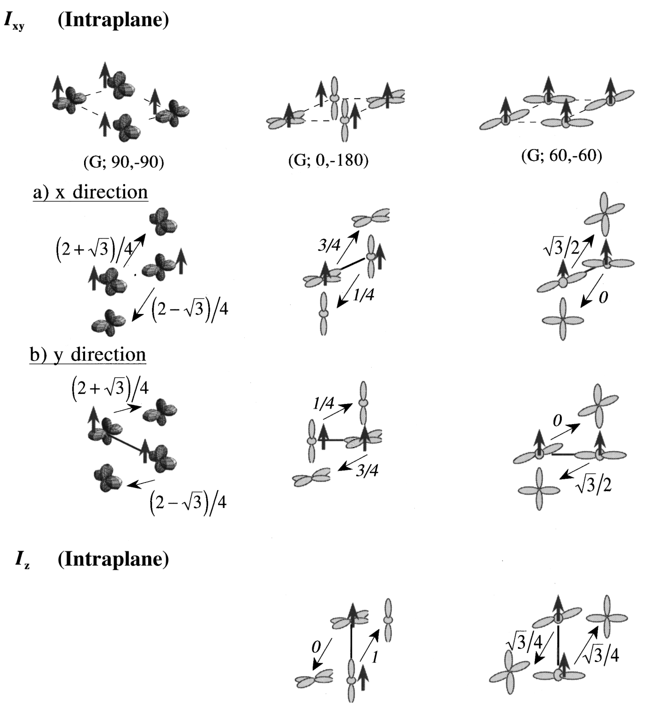

FIG. 8. Magnitude of the transfer integrals for each orbital ordering appearing in the calculation of Eq. (51).

We conclude that $J_S(FA;g)$ increases with decreasing g as shown in Fig. 7(b). This result implies that with relaxing the JT distortion, a frozen orbital configuration is melted from $(\theta_I,\theta_{II})=(60,-60)$, the spin-$F$ phase is stabilized in comparison with the spin-A phase. This is consistent with the experimental results where the spin-A phase is replaced by the spin-F insulator accompanied by a reduction of the JT

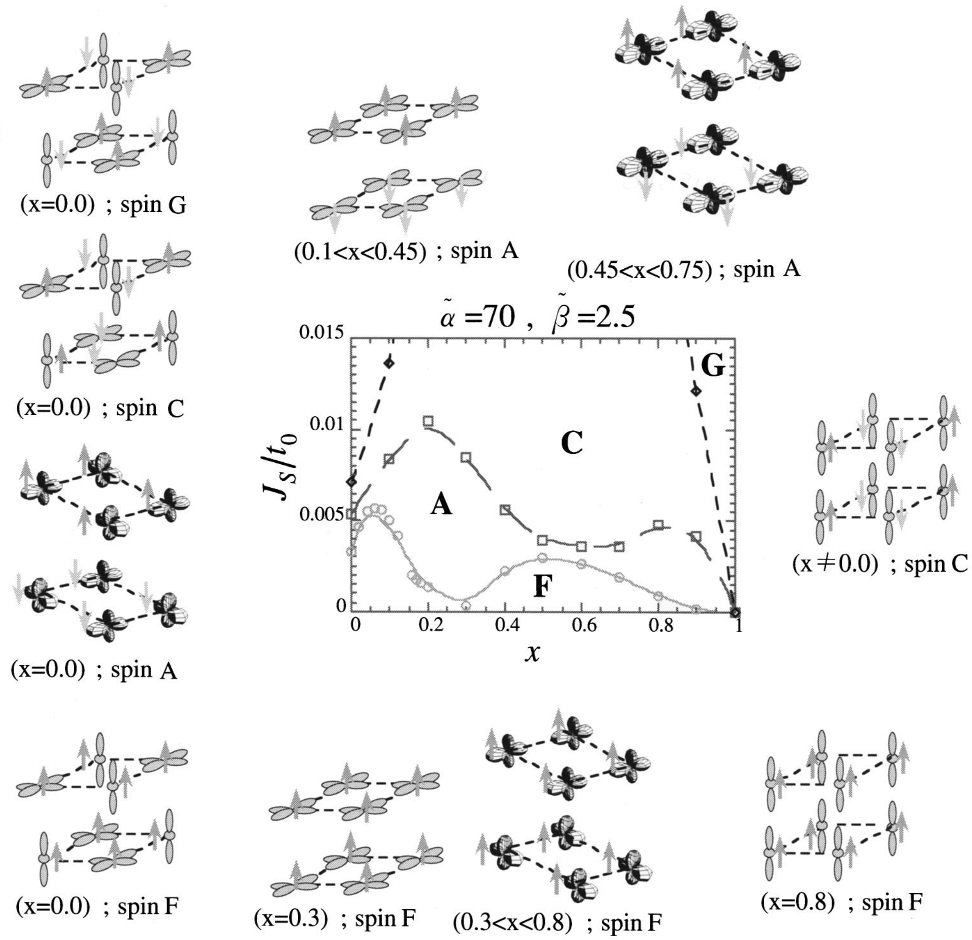

FIG. 9. Mean-field phase diagram as a function of the carrier concentration (x) and the antiferromagnetic interaction between t_{2g} spins (J_S). The energy parameters are chosen to be $\tilde{\alpha}=70$ and $\tilde{\beta}=2.5$ [case (A)]. Schematic orbital structure in the each phase is also shown.

distortion with increasing x, although the present calculation is limited in the undoped case.

D. Doped ($x\neq 0$) case

In this subsection, we show the results in the finite hole-doped case. In Figs. 9 and 10, we present the phase diagrams as a function of hole concentration x in the cases of (A) ($\tilde{\alpha}=70,\tilde{\beta}=2.5$) and (B) ($\tilde{\alpha}=8.1,\tilde{\beta}=6.67$), respectively. The nonmonotonic behavior of the phase boundary is attributed to changes of the orbital structures. In both cases, the global features of phase diagram are almost the same. As discussed before, $\tilde{\alpha}/\tilde{\beta}\gg 1$ corresponds to $U'-J\ll U, U'+J$ and the large Hund coupling. In this limit, the superexchange process for the AF interaction is neglected and the analyses of the calculated results become easier. Therefore, at first, we focus on the results in case (A).

It is found that in nearly the whole doping region except for $x\cong 0$, $(3z^2-r^2)$ and (x^2-y^2) orbital structures are stabilized in the spin-A and C-type phases, respectively, because these orbitals are favorable to maximize a gain of the kinetic energy in each spin structure. A deviation from the (x^2-y^2) structure in the A-type AF phase is found in $0.45<x<0.75$ and is attributed to the hybridization between the occupied and unoccupied bands as discussed later. For spin-G-type AF, the energy does not depend on the orbital so much, because the electron motion is blocked in all directions. In the spin-F structure, on the other hand, the transfer is allowed in any direction. The orbital structure in spin F changes continuously as x increases from orbital G:$(x^2-y^2)/(3z^2-r^2)$ near $x=0$ to orbital F:(x^2-y^2) for $x\sim 0.3$, and to orbital A:$([3z^2-r^2]+[x^2-y^2])/([3z^2-r^2]-[x^2-y^2])$ for $0.3<x<0.8$ and finally orbital F:$(3z^2-r^2)$. The orbital structure is sensitively changed by changing x in comparison with that in the other spin structures.

In order to understand the variation of the spin and orbital structures in the finite hole concentration region, let us consider the density of states (DOS) for each orbital configuration. In Fig. 11, we present the schematic picture of DOS for several values of $\tilde{\alpha}$ and $\tilde{\beta}$. In the case of large $\tilde{\alpha}$ and $\tilde{\beta}$, the density of states is split into four bands. Each band is characterized by the direction of the spin and isospin, that is, the spin is parallel or antiparallel and the isospin is parallel or antiparallel to their mean fields, respectively. It accommodates an electron per site, and the lowest band corresponds to the state where both spin and isospin are parallel. The energy difference between the two bands where the (iso)spin are parallel and antiparallel, respectively, is given by $\tilde{\alpha}\varphi_S=\tilde{\alpha}(1-x)/2\,[\tilde{\beta}\varphi_T=\tilde{\beta}(1-x)/2]$. In the small doped case where $(1-x)\gg t_0/\tilde{\beta}$ is satisfied, the large energy gap ap-

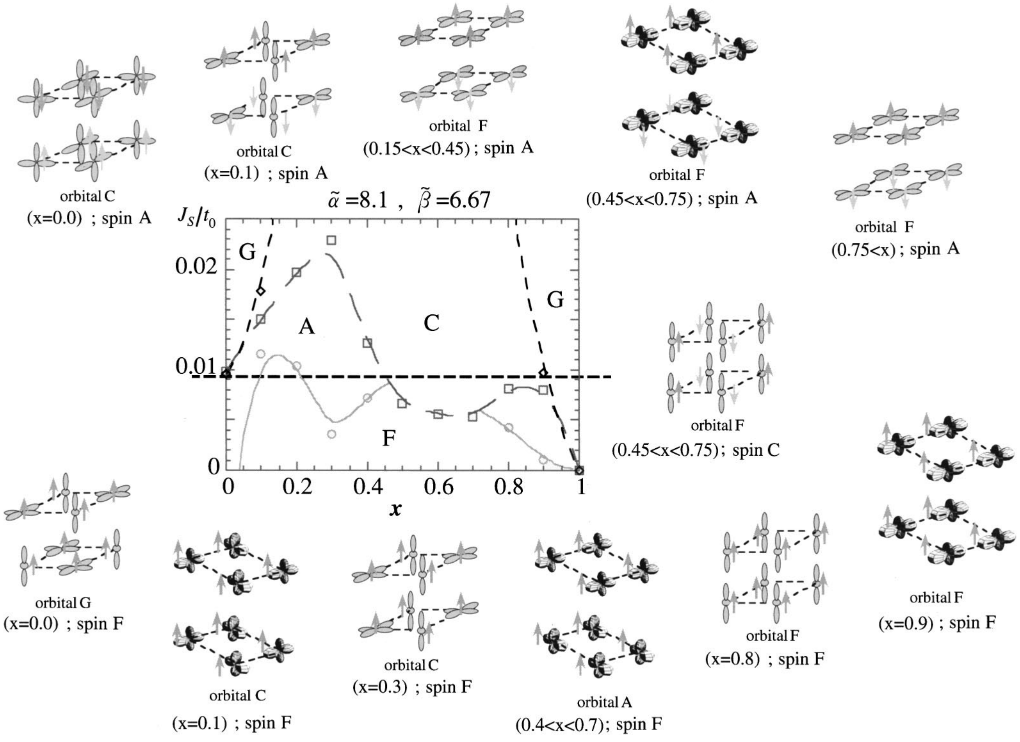

FIG. 10. Mean-field phase diagram as a function of the carrier concentration (x) and the antiferromagnetic interaction between t_{2g} spins (J_S). The energy parameters are chosen to be $\tilde{\alpha}=8.1$ and $\tilde{\beta}=6.67$ [case (B)]. Schematic orbital structure in each phase is also shown. The dotted line $(J_S=0.009)$ reproduces well the change of the spin structure experimentally observed (see text).

pears and the hybridizations between the bands are negligible. The lowest band is therefore constructed almost only from the orbital described by Eq. (34). On the other hand, in the sufficiently large doped case $(1-x)\lesssim t_0/\tilde{\beta}$, the energy gap shrinks and the orbital polarization is reduced. This change of the band gap with varying the hole concentration is able to be detected as the interband transition in the optical measurements.

Next, we demonstrate how the orbital structure controls the dimensionality of DOS. In Fig. 12, we present DOS calculated in several orbital structures. The spin structure is assumed to be F type and the hole concentration is fixed at $x=0$. At first, we focus on the case for orbital $G{:}(x^2-y^2)/(3z^2-r^2)$ and $F{:}(x^2-y^2)$ [Fig. 12(b)] which are realized in $x<0.3$ in the ferromagnetic region as shown in Fig. 9. Results in the both cases are essentially the same. The DOS shows a two-dimensional character, because of the absence of the hopping integral along the c axis. In this case there is no difference in the kinetic energy between spin F and spin A, and J_S favors spin A. This causes a dip structure in the phase boundary between spin F and spin A at $x\sim 0.3$ and leads to a remarkable difference from the prediction by the conventional double-exchange model. In Fig. 12(c), the DOS for the orbital $A{:}([3z^2-r^2]+[x^2-y^2])/([3z^2-r^2]-[x^2-y^2])$ is shown. This orbital structure is stabilized in $0.3<x<0.8$ as shown in Fig. 9. Although the DOS should be essentially three dimensional if there is no hybridization, the result has two peaks which resemble that in the quasi-one-dimensional system [Fig. 12(a)]. This seems to be originated from the hybridization with the unoccupied band. For each case in Fig. 12, the width in the lowest band is the same, as expected in the case of $(1-x)\gg t_0/\tilde{\beta}$. Therefore, by adjusting the orbital structure, the shape of the DOS is modified and the center of mass for the occupied states are changed so as to minimize the kinetic energy. From this viewpoint, a dimensionality of the lowest energy band plays an essential role in the increase of the kinetic energy. In the regions of $x\sim 1$, one-dimensional-like dispersion is advantageous as shown in Fig. 9.

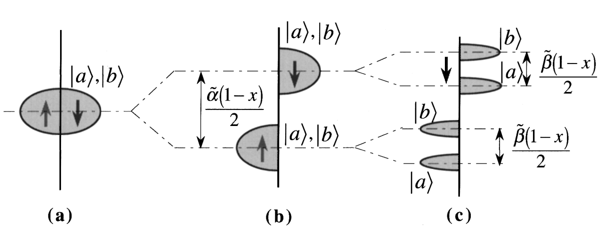

FIG. 11. Splitting of the band structure for e_g electrons. The up and down arrows represent the direction of spin, while $|a\rangle$ and $|b\rangle$ represent one of the e_g orbitals in each band. (a) The $\tilde{\alpha}=\tilde{\beta}=0$ case, (b) the $\tilde{\alpha}\neq 0, \tilde{\beta}=0$ case, and (c) the $\tilde{\alpha}\neq 0, \tilde{\beta}\neq 0$ case.

Let us consider case (B) in Fig. 10 where the more realistic energy parameters are adopted. At the moment, a value of J_S cannot be estimated accurately, but there are two rough estimates. One is from the Néel temperature $T_N=130$ K for $\mathrm{CaMnO_3}\,(x=1.0)$,[11] which suggest $J_S=T_N/7.5\cong 1.7$ meV $\cong 0.0023t_0$ in the mean-field approximation. The fluctuations lower T_N, and hence increase the estimate for J_S. Another estimate is obtained from the numerical calculations for $\mathrm{LaMnO_3}\,(x=0.0)$, which suggests $J_S\cong 8\ \mathrm{meV}\cong 0.011t_0$.[22] Although J_S might depend on x in real materials, we tenta-

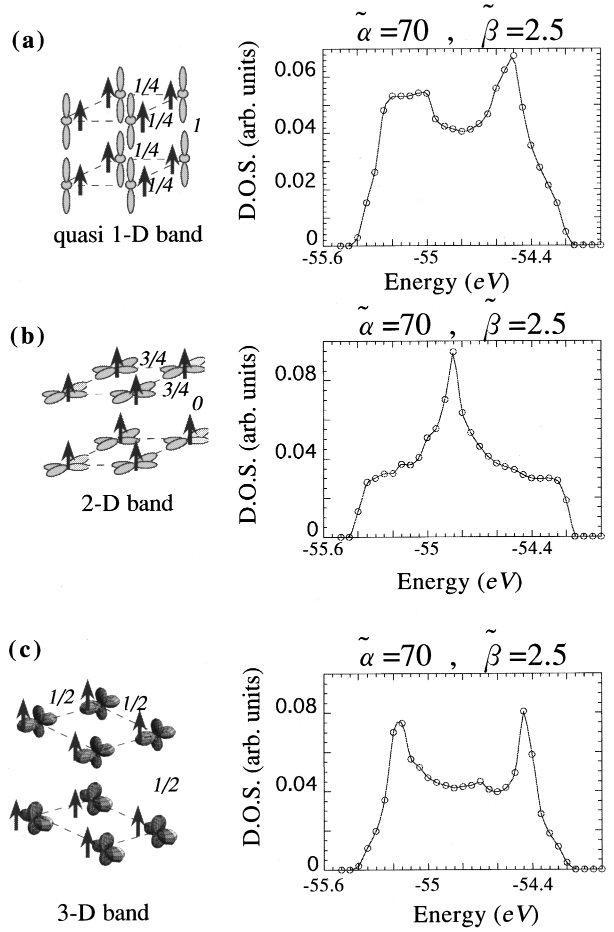

FIG. 12. Density of states of the lowest band at $x=0$. The orbital structures are assumed to be (a) $\theta=180°$ ($d_{3z^2-r^2}$), (b) $\theta=0°$ ($d_{x^2-y^2}$), and (c) $\theta=90°$. The ferromagnetic spin structure is assumed. The energy parameters are chosen to be $\tilde{\alpha}=70$ and $\tilde{\beta}=2.5$ [case (A)]. A value beside each bond represents the transfer intensity.

tively set J_S to $0.009t_0$ represented by the broken line in Fig. 10. Then the spin structure is changed as $A\rightarrow F\rightarrow A\rightarrow C\rightarrow G$, as x increases, which is in good agreement with the experiments shown in Fig. 1(c).

As we mentioned above, the ferromagnetic phase is roughly divided into two regions: the low-doped region ($x<0.3$) and high hole-doped one ($x>0.3$). The former is not reproduced by the calculation without the Coulomb interaction between e_g electrons, on the other hand, the latter is not changed. We conclude that the superexchange interaction discussed in the previous subsection and the conventional double-exchange interaction are dominant in the lower and higher doped regions, respectively. In the present formulation, the character of the superexchange interaction in the metallic phase is derived by the following mechanism. We consider the state where the AF spin structure or the AF orbital structure exist. In this case, the eigenenergy of $M_{kk';\gamma\gamma';\alpha\beta}$ in Eq. (32) corresponding to the Hartree-Fock energy is roughly expressed as $E_k\sim\sqrt{\varepsilon(\vec{k})^2+U_{\rm eff}(x)^2}$, where $\varepsilon(\vec{k})$ and $U_{\rm eff}(x)$ are the diagonal and off-diagonal matrix elements of $M_{kk';\gamma\gamma';\alpha\beta}$, respectively. The former is the order of the transfer intensity and the latter is roughly estimated as $U_{\rm eff}(x)=U_c\varphi\sim U_c(1-x)$. φ is the auxiliary field for the spin and/or isospin degrees and U_c is the order of U. Therefore, the bandwidth of the band is given by $w=E_{\vec{k}=\vec{k}_0}-U_{\rm eff}(x)$. $\vec{k}_0$ is the momentum where $\varepsilon(\vec{k})=0$. It is approximated as t^2/U_c for small x. This result is in contrast to the large x case where the bandwidth is the order of t. As de Gennes has pointed out in the case for small x,[7] the kinetic energy is determined by the product of the bandwidth and the carrier concentration expressed in the present case as $\Delta E\sim wx=(t^2/U_c)x$. We stress that the energy scale t^2/U_c corresponds to that in the superexchange interaction. With increasing x, this ''superexchange character'' in the interaction is gradually replaced by the double-exchange one. Actually, the peak in the phase boundary at $x\sim0.15$ in Fig. 10 grows with increasing t/U_c [Fig. 13(a)], on the other hand, the structure for $x>0.3$ is almost unchanged.

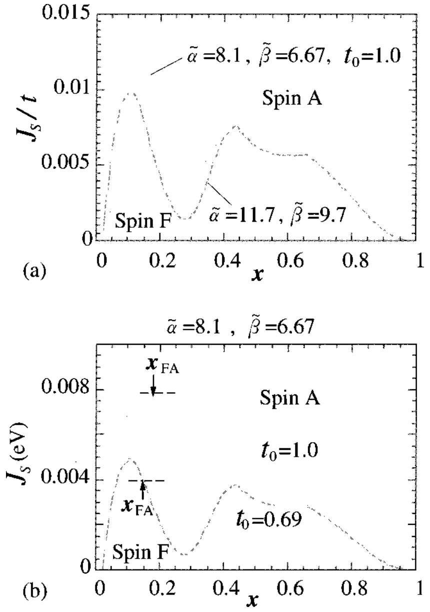

FIG. 13. Variation of the phase boundary $J_S(FA)$ between the spin-F and A phases. (a) Values of the parameters $\tilde{\alpha}$ and $\tilde{\beta}$ are changed. (b) Values of the parameter t_0 are changed. The cross point x_{FA} represents the transition from spin F to spin A, where J_S scales as $J_S\propto t_0^2$.

The modification of the F- and A-spin phases by changing the energy parameters discussed above explains the recent experiment in $({\rm La}_{1-z}{\rm Nd}_z)_{1-x}{\rm Sr}_x{\rm MnO}_3$.[40] The phase transition between the spin-A and spin-F metallic phases was studied by changing the bandwidth, which is controlled by z, and the hole concentration x. With increasing the bandwidth, the critical hole concentration x_{F-A}, where the phase transition occurs, is increased. This experimental result is consistent with the present calculation shown in Fig. 13(b) where t_0 and $J_S\propto t_0^2$ are changed with fixing $\tilde{\alpha}$ and $\tilde{\beta}$. It is found that the critical carrier concentration x_{F-A} is shifted to the higher x region with increasing t_0 as consistent with the experiments.

As shown in Figs. 9 and 10, the orbital structure in the spin-F phase is sensitively changed with the energy parameters and the carrier concentration. This implies that there are many nearly degenerate orbital configurations in this phase.

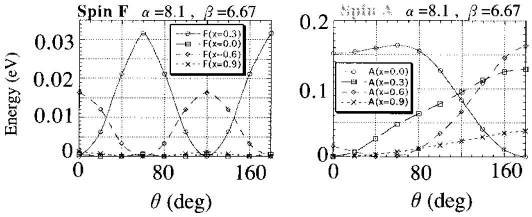

FIG. 14. The energy as a function of the orbital state characterized by θ in several values of x. (a) Spin F is assumed. (b) Spin A is assumed. In both cases, the orbital F-type structure is assumed. The energy parameters are chosen to be $\tilde{\alpha}=8.1$ and $\tilde{\beta}=6.67$ [case (B)].

In order to investigate the situation in detail, we compare the free energies with assuming several orbital structures in the ferromagnetic phase [Fig. 14(a)]. We vary the angle in the orbital space θ with assuming the ferromagnetic orbital configuration. The calculation is also performed in the A-type AF spin case [Fig. 14(b)]. It is found that the energy variation is an order of magnitude smaller in the case of spin F compared with the case of spin A. The difference between the two cases is interpreted from the viewpoint of the anisotropy of the electron transfer under the orbital ordering as follows. In the spin-A case, the (x^2-y^2) orbital is realized to maximize the kinetic energy gain and hopping along the c axis is forbidden. In the spin-F case, on the other hand, such lowering of the dimensionality does not occur because the three crystallographic axes are equivalent in this spin structure. As a result, the orbital configurations have more freedom. This is the same physical idea behind the orbital liquid scenario proposed by the present authors[34] where the two-dimensional orbital fluctuation, characterized by the (x^2-y^2), (y^2-z^2), and (z^2-x^2) orbital alignments, is suggested. Through the orbital fluctuation among them, the kinetic energy in every direction is lowered and the ferromagnetic phase is stabilized. As a results, it is thought that the dip structure in the phase boundary between F- and A-spin structures shown in Fig. 10 disappears and the two ferromagnetic phases in the low- and high-doped regions are connected.

Another possibility, which enhances the ferromagnetism in the region of $x<0.175$ is the JT distortion.[30] In experiments, however, the static JT distortion disappears rapidly with increasing of x around $x\sim 0.1$.[14] Then the dynamical JT distortion should be considered in the metallic spin-F state. According to the study in a large-d model,[41] the large Coulomb interaction is essential to explain both the isotope effect[43] and the Raman-scattering experiment.[42] Then the dominant role of the Coulomb interaction assumed in this paper seems to be reasonable.

One of the most remarkable results in Fig. 10 is an emergence of the spin-A metallic phase for $0.2<x<0.5$ and the spin-C phase for $x>0.5$. These two phases are found in experiments using high-quality samples with narrower bandwidth: $Pr_{1-x}Sr_xMnO_3$ and $Nd_{1-x}Sr_xMnO_3$.[9,10,16] Also in $La_{1-x}Sr_xMnO_3$, a spin-A metallic was recently found to emerge for $x>0.54$.[44] It is worth noting that the metallic spin-A phase is highly in contrast to the spin-A insulating phase observed around $x\sim 0$. An existence of the spin canting in the metallic spin-A phase is theoretically excluded as follows. According to the study by de Gennes,[7] the spin canting from the insulating A-type spin structure lowers the energy by

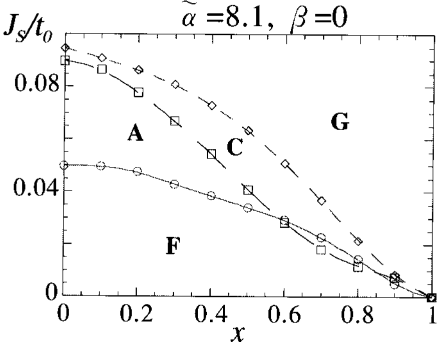

FIG. 15. Mean-field phase diagram calculated assuming $\tilde{\beta}=0$.

$$E_{\mathrm{cant}}=E_A-\frac{Nb_{\mathrm{inter}}^2}{8z|J_S|S^2}x^2, \tag{51}$$

where E_{cant} is the energy in the spin canted phase, b_{inter} is the hopping integral along the c axis, z is the coordinate number along this axis, and N is the number of the ion. The canting angle Θ is given by

$$\cos\frac{\Theta}{2}=\frac{b_{\mathrm{inter}}}{4|J_S|S^2}x. \tag{52}$$

From the consideration, the spin-A phase around $0<x<0.1$ in Fig. 10 is replaced by the spin-canted phase and a value of J_S at the phase boundary is corrected downward as

$$J_S(F-\mathrm{Cant})=J_S(FA)-\frac{Nb_{\mathrm{inter}}^2}{36z|J_S|S^2}x^2. \tag{53}$$

On the other hand, in the spin-A metallic phase $(0.2<x<0.45)$ with the orbital structure (x^2-y^2), the hopping along the c axis is forbidden by the orbital structure and hence no spin canting occurs. This is consistent with the recent neutron-scattering experiment showing no canting in this spin-A metallic phase.[16] Furthermore, the large anisotropy in the resistivity[10] and the distortion of the MnO_6 octahedron[45] observed in the A-type AF at $x=0.60$ and the C-type AF at $x=0.75$ in $Nd_{1-x}Sr_xMnO_3$ are consistent with the calculated orbital structure: (x^2-y^2) for spin A and $(3z^2-r^2)$ in spin C.

IV. DISCUSSION AND CONCLUSIONS

Here we discuss the relation between the present work and the previous ones performed at $x=0.0$. Kugel and Khomskii[21] and Koshibae *et al.*[23] have dealt with the spin and the orbital orderings at $x=0$, taking into account the orbital degeneracy and the electron-electron interactions. They used the effective Hamiltonian obtained by the second-order perturbative expansion in the limit of strong Coulomb repulsion. Kugel and Khomskii studied the ground-state spin and orbital structures in the small limit of J/U' without the antiferromagnetic interaction J_S between t_{2g} spins. In the mean-field calculation, the A-type spin structure is reproduced but the orbital structure is almost of $(z^2-x^2)/(y^2-z^2)$-type ordering, which disagrees with the one expected from a type of the observed JT distortion. On the other hand, Koshibae *et al.* also studied the spin and orbital structures in the large limit of J/U' with taking into account J_S. By using the exact diagonalization method in the finite cluster system, it was found that the spin correlation changes as $F \to A \to C \to G$-type as J_S increases. They also found that in the spin-A phase, the component of $(3x^2-r^2)/(3y^2-r^2)$ or $(z^2-x^2)/(y^2-z^2)$ orbital alignments are enhanced, although both components are not distinguished in the orbital correlation function calculated there. Our calculation covers both of these two cases with the following features; (a) J_S is taken into account. (b) Perturbative expansion is not used, i.e., applicable for any parameters, $\tilde{\alpha}/\tilde{\beta}$, J/U'. (c) Spin and the orbital orderings in the infinite system are studied. As shown in Figs. 1–3, in the limit of $\tilde{\alpha}/\tilde{\beta} \gg 1$, a sequential change of the spin structure with changing J_S is observed. The orbital structure is also rearranged and only in the spin-A AF phase, $(\theta_I, \theta_{II}) = (90°, 270°)$ is stabilized. On the other hand, in the limit of $\tilde{\alpha}/\tilde{\beta} \sim 1$, $(\theta_I, \theta_{II}) = (120°, -120°)$ is stabilized in the spin-A AF phase. Therefore, the results obtained in the previous calculation[21,23] are reproduced by the present calculation in the unified fashion. In addition, our calculation shows that the orbital ordering expected from a type of JT distortion cannot be realized for any value of $\tilde{\alpha}/\tilde{\beta}$. It implies indispensability of the anharmonicity from the JT distortion[20] for proper description at $x=0$. This is in accordance with the results by the Hartree-Fock[28] and the first-principles calculation,[29] except that the spin-A phase is realized even without JT shown as in Fig. 10.

Next, let us pay attention to the doped case. As mentioned above, the perfect polarization of the orbital moment derived by the electron-electron interactions plays an essential role on the spin ordering. It controls the dimensionality of the conduction band through the anisotropy of the transfer intensity. If not, the anisotropy of the conduction band is weakened, because of the large hybridization between the lowest band and the others. As a comparison we show in Fig. 15 a phase diagram without the orbital polarization by assuming $\beta = 0$. The phase diagram is dominated by the ferromagnetic state for reasonable values of J_S, and the nonmonotonic behaviors shown in Figs. 9 and 10 disappear. We conclude that the almost saturated orbital polarization is essential to obtain the experimentally observed phase diagram and the unique character observed in each spin phase, e.g., the two-dimensional conduction and the no spin canting in the metallic A AF phase. For such a large orbital polarization in the metallic phase, the strong Coulomb interaction is indispensable rather than the JT coupling. In the high-T_C cuprates the fluctuation of the full polarized spin moment gives rise to the anomalous properties. It is plausible that the enhanced orbital fluctuation in the spin-F-type metallic state may play a similar role as the origin of anomalous properties observed in the CMR region in the compounds mentioned in Sec. I.[34]

In summary, we have studied the phase diagram of $R_{1-x}A_x\mathrm{MnO}_3$ at zero temperature in the plane of x (hole concentration) and J_S (AF exchange interaction between t_{2g} spins) in the mean-field approximation. The global features are understood in terms of the superexchange interaction and the double-exchange interaction, which is considerably modified from the conventional one due to the strong correlation and the orbital degeneracy. The large orbital polarization originated from the electron-electron interaction is indispensable to reproducing the phase diagram experimentally observed.

ACKNOWLEDGMENTS

The authors would like to thank S. Maekawa, Y. Tokura, K. Terakura, Y. Moritomo, and I. Solovyev for their valuable discussions. This work was supported by Priority Areas Grants from the Ministry of Education, Science and Culture of Japan, and the New Energy and Industrial Technology Development Organization (NEDO).

---

*Present address: Institute for Materials Research, Tohoku University, Sendai, 980-8577, Japan.

[1] K. Chahara, T. Ohono, M. Kasai, Y. Kanke, and Y. Kozono, Appl. Phys. Lett. **62**, 780 (1993).

[2] R. von Helmolt, J. Wecker, B. Holzapfel, L. Schultz, and K. Samwer, Phys. Rev. Lett. **71**, 2331 (1993).

[3] Y. Tokura, A. Urushibara, Y. Moritomo, T. Arima, A. Asamitsu, G. Kido, and N. Furukawa, J. Phys. Soc. Jpn. **63**, 3931 (1994); A. Urushibara, Y. Moritomo, T. Arima, A. Asamitsu, G. Kido, and Y. Tokura, Phys. Rev. B **51**, 14 103 (1995).

[4] S. Jin, T. H. Tiefel, M. McCormack, R. A. Fastnacht, R. Ramesh, and L. H. Chen, Science **264**, 413 (1994).

[5] C. Zener, Phys. Rev. **82**, 403 (1951).

[6] P. W. Anderson and H. Hasegawa, Phys. Rev. **100**, 675 (1955).

[7] P. G. de Gennes, Phys. Rev. **118**, 141 (1960).

[8] G. H. Jonker and H. van Santen, Physica (Amsterdam) **16**, 337 (1950).

[9] Y. Tomioka (unpublished).

[10] H. Kuwahara, T. Okuda, Y. Tomioka, T. Kimura, A. Asamitsu, and Y. Tokura, *Phase Diagram and Anisotropic Transport Properties of* $Nd_{1-x}Sr_xMnO_3$ *Crystals*, MRS Symposia Proceedings No. 494 (Material Research Society, Pittsburgh, 1998), p. 83.

[11] E. O. Wollan and W. C. Koehler, Phys. Rev. **100**, 545 (1955).

[12] G. Matsumoto, J. Phys. Soc. Jpn. **29**, 606 (1970).

[13] T. Okuda, A. Asamitsu, Y. Tomioka, T. Kimura, Y. Taguchi, and Y. Tokura (unpublished).

[14] H. Kawano, R. Kajimoto, M. Kubota, and H. Yoshizawa, Phys. Rev. B **53**, R14 709 (1996); **53**, 2202 (1996).

[15] Y. Moritomo, T. Akimoto, A. Nakamura, K. Ohoyama, and M. Ohashi, Phys. Rev. B **58**, 5544 (1998).

[16] H. Kawano, R. Kajimoto, H. Yoshizawa, Y. Tomioka, H. Kuwahara, and Y. Tokura, Phys. Rev. Lett. **78**, 4253 (1997).

[17] Z. Jirak, S. Krupicka, Z. Simsa, M. Dlouha, and S. Vratislav, J. Magn. Magn. Mater. **53**, 153 (1985).

[18] S. Mori, C. H. Chen, and S.-W. Cheong, Nature (London) **392**, 473 (1998).

[19] J. B. Goodenough, Phys. Rev. **100**, 564 (1955).

[20] J. Kanamori, J. Appl. Phys. **31**, 14S (1960).

[21] K. I. Kugel and D. I. Khomskii, Zh. Eksp. Teor. Fiz. Pis. Red. **15**, 629 (1972) [JETP Lett. **15**, 446 (1972)]; D. I. Khomskii and K. I. Kugel, Solid State Commun. **13**, 763 (1973).

[22] S. Ishihara, J. Inoue, and S. Maekawa, Physica C **263**, 130 (1996); Phys. Rev. B **55**, 8280 (1997).

[23] W. Koshibae, Y. Kawamura, S. Ishihara, S. Okamoto, J. Inoue, and S. Maekawa, J. Phys. Soc. Jpn. **66**, 957 (1997).

[24] R. Shiina, T. Nishitani, and H. Shiba, J. Phys. Soc. Jpn. **66**, 3159 (1997).

[25] L. M. Roth, Phys. Rev. **149**, 306 (1966).

[26] S. Inagaki, J. Phys. Soc. Jpn. **39**, 596 (1975).

[27] M. Cyrot and C. Lyon-Caen, J. Phys. (Paris) **36**, 253 (1975).

[28] T. Mizokawa and A. Fujimori, Phys. Rev. B **51**, 12 880 (1996); **54**, 5368 (1996).

[29] N. Hamada, H. Sawada, and K. Terakura, in *Spectroscopy of Mott Insulators and Correlated Metals*, Solid State Sciences 119 (Springer-Verlag, Berlin, 1995); I. Solovyev, N. Hamada, and K. Terakura, Phys. Rev. Lett. **76**, 4825 (1996).

[30] A. J. Millis, P. B. Littlewood, and B. I. Shraiman, Phys. Rev. Lett. **74**, 5144 (1995).

[31] Y. Okimoto, T. Katsufuji, T. Ishikawa, A. Urushibara, T. Arima, and Y. Tokura, Phys. Rev. Lett. **75**, 109 (1995).

[32] D. D. Sarma, N. Shanthi, S. R. Krishnakurmar, T. Saitoh, T. Mizokawa, A. Sekiyama, K. Kobayashi, A. Fujimori, E. Weschke, R. Meier, G. Kaindl, Y. Takeda, and M. Takano, Phys. Rev. B **53**, 6873 (1996).

[33] R. Maezono, S. Ishihara, and N. Nagaosa, Phys. Rev. B **57**, R13 993 (1998).

[34] S. Ishihara, M. Yamanaka, and N. Nagaosa, Phys. Rev. B **56**, 686 (1997).

[35] T. Saitoh, A. E. Bocquet, T. Mizokawa, H. Namatame, A. Fujimori, M. Abbate, Y. Takeda, and M. Takano, Phys. Rev. B **51**, 13 942 (1995).

[36] M. C. Martin, G. Shirane, Y. Endoh, K. Hirota, Y. Moritomo, and Y. Tokura, Phys. Rev. B **53**, 14 285 (1996).

[37] W. A. Harrison, in *Electronic Structure and the Properties of Solids, The Physics of the Chemical Bond* (Freeman, San Francisco, 1980).

[38] Y. Murakami, H. Kawada, H. Kawata, M. Tanaka, T. Arima, Y. Moritomo, and Y. Tokura, Phys. Rev. Lett. **80**, 1932 (1998).

[39] S. Ishihara and S. Maekawa, Phys. Rev. Lett. **80**, 3799 (1998).

[40] T. Akimoto, Y. Maruyama, Y. Moritomo, A. Nakamura, K. Hirota, K. Ohoyama, and M. Ohashi, Phys. Rev. B **57**, R5594 (1998).

[41] N. Nagaosa, S. Murakami, and H. C. Lee, Phys. Rev. B **57**, R6767 (1998).

[42] K. Yamamoto and Y. Tokura (unpublished).

[43] G. Zhao, K. Conder, H. Keller, and K. A. Muller, Nature (London) **381**, 676 (1996).

[44] Y. Moritomo, H. Kuwahara, Y. Tomioka, and Y. Tokura, Phys. Rev. B **55**, 7549 (1997).

[45] R. Kajimoto, H. Yoshizawa, H. Kawano, H. Kuwahara, Y. Tokura, K. Ohoyama, and M. Ohashi (unpublished).